

## Accepted Manuscript

Characterization of Artifacts Introduced by the Empirical Volcano-Scan Atmospheric Correction Commonly Applied to CRISM and OMEGA Near-Infrared Spectra

S.M. Wiseman, R.E. Arvidson, M.J. Wolff, M.D. Smith, F.P. Seelos, F. Morgan, S.L. Murchie, J.F. Mustard, R.V. Morris, D. Humm, P.C. McGuire

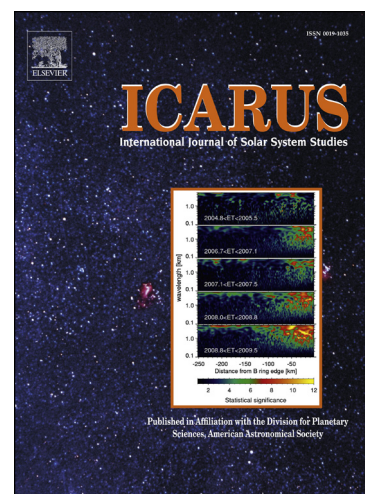
PII: S0019-1035(14)00551-X  
DOI: <http://dx.doi.org/10.1016/j.icarus.2014.10.012>  
Reference: YICAR 11312

To appear in: *Icarus*

Received Date: 3 May 2013  
Revised Date: 3 October 2014  
Accepted Date: 7 October 2014

Please cite this article as: Wiseman, S.M., Arvidson, R.E., Wolff, M.J., Smith, M.D., Seelos, F.P., Morgan, F., Murchie, S.L., Mustard, J.F., Morris, R.V., Humm, D., McGuire, P.C., Characterization of Artifacts Introduced by the Empirical Volcano-Scan Atmospheric Correction Commonly Applied to CRISM and OMEGA Near-Infrared Spectra, *Icarus* (2014), doi: <http://dx.doi.org/10.1016/j.icarus.2014.10.012>

This is a PDF file of an unedited manuscript that has been accepted for publication. As a service to our customers we are providing this early version of the manuscript. The manuscript will undergo copyediting, typesetting, and review of the resulting proof before it is published in its final form. Please note that during the production process errors may be discovered which could affect the content, and all legal disclaimers that apply to the journal pertain.



**Characterization of Artifacts Introduced by the Empirical Volcano-Scan Atmospheric Correction Commonly Applied to CRISM and OMEGA Near-Infrared Spectra**

S. M. Wiseman<sup>1</sup>, R. E. Arvidson<sup>2</sup>, M. J. Wolff<sup>3</sup>, M. D. Smith<sup>4</sup>, F. P. Seelos<sup>5</sup>, F. Morgan<sup>5</sup>, S. L. Murchie<sup>5</sup>, J. F. Mustard<sup>1</sup>, R. V. Morris<sup>6</sup>, D. Humm<sup>7</sup>, P. C. McGuire<sup>8,5</sup>

<sup>1</sup>Department of Earth, Environmental and Planetary Sciences, Brown University, Providence, RI, USA.

<sup>2</sup>McDonnell Center for the Space Sciences, Department of Earth and Planetary Sciences, Washington University in Saint Louis, Saint Louis, Missouri, USA.

<sup>3</sup>Space Science Institute, Boulder, Colorado, USA.

<sup>4</sup>NASA Goddard Space Flight Center, Greenbelt, Maryland, USA.

<sup>5</sup>Johns Hopkins University Applied Physics Laboratory, Laurel, Maryland, USA.

<sup>6</sup>NASA Johnson Space Center, Houston, Texas, USA.

<sup>7</sup>Space Instrument Calibration Consulting, Annapolis, MD, USA.

<sup>8</sup>Planetary Sciences and Remote Sensing Group, Institute of Geological Sciences, Freie Universitaet Berlin, Berlin, Germany.

**Corresponding Author Contact Information:**

Sandra M. Wiseman  
Department of Earth, Environmental and Planetary Sciences  
Brown University  
324 Brook St., Box 1846  
Providence, RI 02912, USA  
Telephone: (401) 863-9663  
Fax: (401) 863-3978  
Email: sandra\_wiseman@brown.edu

## Characterization of Artifacts Introduced by the Empirical Volcano-Scan Atmospheric Correction Commonly Applied to CRISM and OMEGA Near Infrared Spectra

S. M. Wiseman, R. E. Arvidson, M. J. Wolff, M. D. Smith, F. P. Seelos, F. Morgan, R. V. Morris, J. F. Mustard, D. Humm, S. L. Murchie, P. C. McGuire

### 1 Abstract

2           The empirical ‘volcano-scan’ atmospheric correction is widely applied to Martian near  
3 infrared CRISM and OMEGA spectra between ~1000 and ~2600 nm to remove prominent  
4 atmospheric gas absorptions with minimal computational investment. This correction method  
5 employs division by a scaled empirically-derived atmospheric transmission spectrum that is  
6 generated from observations of the Martian surface in which different path lengths through the  
7 atmosphere were measured and transmission calculated using the Beer-Lambert Law.  
8 Identifying and characterizing both artifacts and residual atmospheric features left by the  
9 volcano-scan correction is important for robust interpretation of CRISM and OMEGA volcano-  
10 scan corrected spectra. In order to identify and determine the cause of spectral artifacts  
11 introduced by the volcano-scan correction, we simulated this correction using a multiple  
12 scattering radiative transfer algorithm (DISORT). Simulated transmission spectra that are  
13 similar to actual CRISM- and OMEGA-derived transmission spectra were generated from  
14 modeled Olympus Mons base and summit spectra. Results from the simulations were used to  
15 investigate the validity of assumptions inherent in the volcano-scan correction and to identify  
16 artifacts introduced by this method of atmospheric correction. We found that the most prominent  
17 artifact, a bowl-shaped feature centered near 2000 nm, is caused by the inaccurate assumption  
18 that absorption coefficients of CO<sub>2</sub> in the Martian atmosphere are independent of column  
19 density. In addition, spectral albedo and slope are modified by atmospheric aerosols. Residual  
20 atmospheric contributions that are caused by variable amounts of dust aerosols, ice aerosols, and

21 water vapor are characterized by the analysis of CRISM volcano-scan corrected spectra from the  
22 same location acquired at different times under variable atmospheric conditions.

## 23 **1 Introduction**

24 Images of the Martian surface acquired by the NASA Mars Reconnaissance Orbiter  
25 (MRO) Compact Reconnaissance Imaging Spectrometer for Mars (CRISM) [Murchie *et al.*,  
26 2007] and the Mars Express Observatoire pour la Minéralogie, l'Eau, les Glaces et l'Activité  
27 (OMEGA) [Bibring *et al.*, 2004; 2005] measure solar light that was attenuated and scattered as it  
28 traversed down through the Martian atmosphere, interacted with the surface, and traversed up  
29 through the atmosphere. Therefore, each spectrum from standard CRISM and OMEGA  
30 observations contains contributions from atmospheric gases (e.g., CO<sub>2</sub>, CO, and H<sub>2</sub>O),  
31 atmospheric aerosols (e.g., dust and water ice), and the surface. Atmospheric gas contributions  
32 dominate the spectrum at wavelengths that CO<sub>2</sub> absorbs (Figure 1).

33 The empirical 'volcano-scan' correction [Bibring *et al.*, 1989; Langevin *et al.*, 2005;  
34 McGuire *et al.*, 2009] is widely applied to CRISM and OMEGA near infrared (NIR) spectra  
35 between ~1000 and ~2600 nm to remove prominent atmospheric gas absorptions with minimal  
36 computational investment. The volcano-scan correction method employs division by a scaled  
37 atmospheric transmission spectrum that is generated from observations of the Martian surface in  
38 which different path lengths through the atmosphere were measured. Low and high altitude  
39 spectra acquired over the base and summit of the Olympus Mons volcano were used, giving the  
40 correction its name. Transmission is calculated empirically using the Beer-Lambert Law, as  
41 detailed in section 2.2.

42           Although the volcano-scan correction removes prominent gas absorptions to first order,  
43 closer inspection reveals that corrected spectra exhibit spurious features in areas of strong gas  
44 absorption. The most prominent artifact is a bowl-shaped feature that overlaps with the CO<sub>2</sub>  
45 triplet centered near 2000 nm (Figure 1). The volcano-scan correction can be applied  
46 automatically to CRISM images using publically available CRISM Analysis Tools (CAT)  
47 software released through the Planetary Data System (PDS). The current version of CAT at this  
48 time (version 7.2.1) includes an option to empirically correct the 2000 nm bowl-shaped artifact  
49 that is evident in volcano-scan corrected images on a pixel by pixel basis.

50           The occurrence of the apparent bowl-shaped artifact at 2000 nm could have several  
51 causes. There are three major assumptions implicit in deriving empirical transmission spectra: 1)  
52 surface contributions to the low and high altitude spectra used to create transmission spectra are  
53 equivalent and therefore cancel out, 2) aerosol contributions to low and high altitude spectra can  
54 be ignored both within and outside of gas absorption lines and therefore empirical transmission  
55 spectra contain molecular absorption only, 3) absorption coefficients of CO<sub>2</sub> in the Martian  
56 atmosphere are independent of column density and absorption strength therefore scales  
57 exponentially with column density.

58           In order to identify and determine the cause of artifacts introduced by the volcano-scan  
59 correction method, we simulated this correction using a multiple scattering radiative transfer  
60 algorithm. Discrete Ordinate Radiative Transfer (DISORT) modeling allows for the explicit  
61 treatment of aerosol, gas, and surface contributions simultaneously [*Stamnes et al.*, 1988;  
62 *Thomas and Stamnes*, 2002]. The DISORT radiative transfer model was used to calculate  
63 modeled high and low altitude spectra similar to Martian spectra of Olympus Mons. Simulated  
64 transmission spectra were derived from these modeled spectra using the same method that was

65 used to produce CRISM- and OMEGA-derived transmission spectra. Generating simulated  
66 transmission spectra in this manner and applying them to modeled Martian spectra using the  
67 volcano-scan correction method allows the variables related to the three major assumptions  
68 described above to be controlled and analyzed.

69 Because the volcano-scan correction is designed to remove absorptions from atmospheric  
70 CO<sub>2</sub>, this correction does not specifically address contribution from other atmospheric species,  
71 including dust and ice aerosols and gaseous water vapor. CO absorption is minor (Figure 1, gray  
72 arrow) and will not be considered. Aerosol and water vapor atmospheric contributions are  
73 particularly important because they are spatially and temporally variable [e. g., *Smith et al.*,  
74 2008] and produce noticeable features in CRISM and OMEGA spectra [e. g., *Smith et al.*, 2009].  
75 Dust aerosol contributions affect spectral slope and amplitude and ice aerosols also have distinct  
76 absorption features in the NIR. In addition, aerosol scattering within gas absorption lines alters  
77 absorption features. Atmospheric water vapor absorptions that occur in empirically derived  
78 transmission spectra cannot be scaled separately from CO<sub>2</sub> absorptions in the transmission  
79 spectrum that is scaled during the volcano-scan correction. Failure to explicitly address  
80 atmospheric water vapor can cause under- and over-corrected water vapor features in volcano-  
81 scan corrected spectra.

82 Identifying and characterizing both artifacts and residual atmospheric features left by the  
83 volcano-scan correction is important for proper interpretation of CRISM and OMEGA volcano-  
84 scan corrected spectra. Results from the simulated volcano-scan correction are used to  
85 investigate the validity of assumptions inherent in deriving and applying empirical transmission  
86 spectra and to identify and determine the causes of artifacts (e.g., 2000 nm bowl-shape)  
87 introduced by this atmospheric correction method. In addition, we characterize spectral features

88 that result from dust aerosols, ice aerosols, and water vapor that are not specifically addressed by  
89 the volcano-scan correction. Variations in these species cause volcano-scan corrected spectra to  
90 exhibit variable residual features depending on atmospheric conditions at the time of image  
91 acquisition. These residual features and artifacts are highlighted by comparison of CRISM  
92 volcano-scan corrected spectra from the same location on Mars but acquired at different times  
93 under variable atmospheric conditions.

## 94 **2 Background**

### 95 **2.1 CRISM and OMEGA Datasets**

96 The CRISM spectrometer has short (S) and long (L) wavelength detectors that operate  
97 between 360 to 1053 nm and 1003 to 3920 nm, respectively [Murchie *et al.*, 2007; 2009].  
98 CRISM is capable of acquiring hyperspectral images with 544 channels spaced ~7 nm apart.  
99 CRISM is mounted on a gimbal platform that allows ground tracking of a target to acquire full  
100 resolution targeted (FRT) images with up to 20 m/pixel spatial resolution. The CRISM  
101 spectrometer utilizes 2-dimensional detector arrays that cause slight column dependencies in  
102 CRISM spectral data, including a smooth variation in the central wavelength position of each  
103 channel [Murchie *et al.*, 2007]. Image rows are built up as a result of along track spacecraft  
104 motion. CRISM I/F (where I is the radiance at sensor divided by the solar irradiance, F, at the  
105 top of the Martian atmosphere divided by  $\pi$ ) spectra available from the PDS ([http://pds-  
106 geoscience.wustl.edu](http://pds-geoscience.wustl.edu)) were calibrated as described by Murchie *et al.* [2007, 2009].

107 Atmospheric transmission files derived from CRISM hyperspectral, non-gimbaled FFC  
108 images acquired at the base and summit of Olympus Mons are contained in Atmospheric  
109 Transmission (AT) Calibration Data Record (CDR) files that are available through the PDS.

110 Because a relatively small ( $< 1.5$  nm) temperature dependent wavelength shift is observed in  
111 CRISM L detector spectra [Smith *et al.*, 2009], AT CDRs for several different wavelength shifts  
112 were derived. A slope correction was applied to transmission spectra in the AT CDR files in an  
113 effort to normalize the shapes of the transmission spectra and ensure that continuum values are  
114 near unity. The most current version of CAT at this time (version 7.2.1) includes an option to  
115 empirically correct the 2000 nm bowl-shaped artifact that is evident in volcano-scan corrected  
116 images on a pixel by pixel basis (algorithm developed by Frank Morgan and formulation present  
117 in CAT v7.2.1 code). The 2000 nm bowl-shaped artifact is defined relative to a straight line  
118 continuum derived from a reference observation. The same low altitude Olympus Mons spectra  
119 used to generate empirical transmission spectra are used to define the artifact (to minimize  
120 temperature dependent wavelength shift and surface variations) for wavelengths between  $\sim 1760$   
121 and 2240 nm. The artifact correction spectrum is determined by subtracting the volcano-scan  
122 corrected reference spectrum from the continuum fit to that spectrum. After the volcano-scan  
123 correction is applied, the artifact correction spectrum is multiplicatively scaled to match the  
124 artifact expressed in each pixel. The 2000 nm bowl-shaped artifact is then corrected by adding  
125 the scaled artifact correction to the volcano-scan corrected spectrum, for each pixel in the image.

126 The OMEGA spectrometer [Bibring *et al.*, 2004] covers the wavelength range from 350  
127 to 5100 nm in 352 channels using VNIR (350 to 1070 nm), C (930 to 2700 nm), and L (2530 to  
128 5100 nm) detectors. C detector channels have a wavelength spacing of  $\sim 14$  nm [Bibring *et al.*  
129 2004, 2005]. Images vary in spatial resolution depending on spacecraft altitude and are built up  
130 by across track scanning and along track spacecraft motion. OMEGA data lack the column  
131 dependent issues inherent in CRISM data. OMEGA images as well as software to calibrate and  
132 process the images to units of I/F as described by Bibring *et al.* [2004, 2005], are available



133 through the PDS at <http://pds-geoscience.wustl.edu>. An OMEGA-derived atmospheric  
 134 transmission spectrum for use with the empirical volcano-scan correction is not publically  
 135 available but can be calculated from Olympus Mons observations using methods described in the  
 136 following section.

## 137 2.2 Empirical Volcano-Scan Correction

138 The empirical volcano-scan correction method relies on empirically derived transmission  
 139 spectra to remove CO<sub>2</sub> absorption features from spectra of the Martian surface [*Bibring et al.*,  
 140 1989; *Langevin et al.*, 2005; *McGuire et al.*, 2009]. Transmission spectra are generated from  
 141 observations in which different path lengths through the atmosphere were measured. High  
 142 altitude spectra were acquired at the summit of Olympus Mons (~20 km above datum) and low  
 143 altitude spectra at its base (~0 km) (Figure 2a). Transmittance between the base and summit of  
 144 Olympus Mons is determined using the Beer-Lambert Law (equation 1) integrated with the  
 145 assumption that the absorption coefficient,  $k$ , is constant with height in the atmosphere (equation  
 146 2).

$$147 \quad T(\lambda) = I_{\lambda}(s_{0 \rightarrow 2}) / I_{\lambda}(s_{0 \rightarrow 1}) = e^{-\int_{s_1}^{s_2} k ds} \quad (1)$$

$$148 \quad T(\lambda) = I_{\lambda}(s_{0 \rightarrow 2}) / I_{\lambda}(s_{0 \rightarrow 1}) = e^{-k s_{1 \rightarrow 2}} = e^{-\tau} \quad (2)$$

$$149 \quad -\ln(T(\lambda)) = k s_{1 \rightarrow 2} = \tau \quad (3)$$

150  
 151 In equations 1 through 3,  $T$  is transmittance,  $I_{\lambda}$  is equivalent to CRISM or OMEGA I/F at  
 152 wavelength ( $\lambda$ ),  $s_{0 \rightarrow 1}$  is the sum of the incoming and outgoing path lengths from the top of the  
 153 atmosphere ( $s_0$ ) to height  $s_1$  within the atmosphere,  $s_{0 \rightarrow 2}$  is the sum of the incoming and outgoing

154 path lengths from the top of the atmosphere ( $s_0$ ) to height  $s_2$  within the atmosphere, and  $\tau$  is the  
155 total extinction. Note, for nonzero solar incidence ( $i$ ) angles or detector emission ( $e$ ) angles, the  
156 incoming path length is equal to the height ( $s_0$  or  $s_1$ ) divided by  $\cos(i)$  and the outgoing path  
157 length is the height divided by  $\cos(e)$ . Implicit in equation (2) is that the surface contribution to  
158  $I_\lambda(s_{0 \rightarrow 1})$  and  $I_\lambda(s_{0 \rightarrow 2})$  is identical and that  $k$  is independent of path length ( $s$ ). The effects of  
159 aerosol scattering within wavelengths of gas absorption are ignored for the purposes of deriving  
160 empirical transmission spectra and  $\tau$  is assumed to result from molecular absorption only.  
161 Although  $T$  at wavelengths outside of gas bands should equal unity, in practice, the ratio of the  
162 low and high altitude spectra must be multiplicatively scaled to  $\sim 1.0$  at wavelengths outside of  
163 gas absorptions to account for differences in surface spectral features and/or aerosol opacities in  
164 high and low altitude spectra.

165 To perform the volcano-scan correction for an arbitrary CRISM or OMEGA I/F  
166 spectrum, the empirically derived transmission spectrum is scaled using an exponential factor  
167 determined so that the most prominent  $\text{CO}_2$  absorption feature in the transmission spectrum has  
168 an equivalent depth to the same  $\text{CO}_2$  feature in the I/F spectrum that is to be corrected, as  
169 described below. For simplicity, the 'I/F spectrum that is to be corrected' will be referred to as  
170 the target I/F spectrum. That is, division of the surface spectrum by the scaled transmission  
171 spectrum, in principle, eliminates  $\text{CO}_2$  absorption features from the target I/F spectrum. During  
172 application of the volcano-scan correction, the transmission spectrum must be scaled separately  
173 for each target I/F spectrum because the surface pressure, which affects the depth of  $\text{CO}_2$   
174 absorptions, varies as a function of surface elevation and solar longitude ( $L_s$ ) (e. g., *Smith et al.*,  
175 2004). Calculating the exponential scaling factor that is needed for the most prominent  $\text{CO}_2$   
176 feature in the transmission spectrum to match up with the depth of the same  $\text{CO}_2$  feature in the

177 target I/F spectrum relies on band depth estimates. The band depth of an absorption feature in  
 178 the target I/F spectrum and the band depth of the same feature in the empirical transmission  
 179 spectrum are proxies for the transmittance that occurred over the atmospheric path lengths  
 180 traversed for the I/F target spectrum and the empirical transmission spectrum, respectively. In  
 181 the equations below, the arbitrary CRISM or OMEGA I/F spectrum that is to be corrected is  
 182 labeled ‘target’, the transmission spectrum is labeled ‘trans’,  $I_{\text{feature}}$  is the I/F value of a CO<sub>2</sub>  
 183 absorption feature at some wavelength,  $T_{\text{feature}}$  is the transmission value of a CO<sub>2</sub> absorption  
 184 feature at the same wavelength, and BD is the band depth of that CO<sub>2</sub> feature. The target I/F  
 185 spectrum has an arbitrary atmospheric path length of  $s_{0 \rightarrow 3}$ .

$$186 \quad BD_{\text{targ}} = I_{\text{feature}}(\text{target})/I_{\text{continuum}}(\text{target}), \quad (4)$$

187 assuming  $T=1$  on the continuum,

$$188 \quad BD_{\text{targ}} = I_{\text{feature}}(s_{0 \rightarrow 3})/I_{\text{continuum}} = e^{-ks_{0 \rightarrow 3}}, \quad (5)$$

189 Similarly,

$$190 \quad BD_{\text{trans}} = T_{\text{feature}}(\text{trans})/T_{\text{continuum}}(\text{trans}), \quad (6)$$

$$191 \quad BD_{\text{trans}} = T_{\text{feature}}(s_{1 \rightarrow 2})/T_{\text{continuum}} = e^{-ks_{1 \rightarrow 2}}. \quad (7)$$

192 The exponential scaling factor is determined from

$$193 \quad \ln(BD_{\text{targ}})/\ln(BD_{\text{trans}}) = \ln(e^{-ks_{0 \rightarrow 3}})/\ln(e^{-ks_{1 \rightarrow 2}}) = s_{0 \rightarrow 3}/s_{1 \rightarrow 2}. \quad (8)$$

194 Because the exponential scaling factor represents the difference in path length between  
 195 the target spectrum and the transmission spectrum, its value should be the same for all

196 wavelengths. However, uncertainties are associated with determining the band depth from  
 197 CRISM spectra. An estimate of the band depth for the strongest CO<sub>2</sub> band in the CO<sub>2</sub> triplet near  
 198 2000 nm is commonly calculated as the ratio of the slope corrected I/F value along the  
 199 continuum at ~1900 nm to the I/F value in the CO<sub>2</sub> absorption feature at ~2010 nm. OMEGA  
 200 measures only a single channel near 2010 nm, which is located at 2012 nm, whereas CRISM has  
 201 channels at 2007 and 2014 nm. *McGuire et al.*, [2009] note that variations in the surface spectral  
 202 contribution between the wavelength along the continuum and the wavelength of the CO<sub>2</sub>  
 203 absorption feature can cause error in the calculated band depth and instead suggests using the  
 204 ratio of the I/F continuum value at 1980 nm to the I/F value of the CO<sub>2</sub> absorption feature at  
 205 2007 nm. These two band depth estimates will be referred to as the BD1 and BD2, respectively.  
 206 All wavelengths of the transmission spectrum are scaled by the single (wavelength independent)  
 207 exponential factor calculated using the band depth estimate.

208 Applying the volcano-scan correction to the target spectrum of interest, remembering that

$$209 \quad I_{\lambda}(s_{0 \rightarrow 3}) = I_{\lambda}(s_0) * e^{-ks_{0 \rightarrow 3}}, \quad (9)$$

210 results in

$$211 \quad I_{feature}(s_0) e^{-ks_{0 \rightarrow 3}} / (e^{-ks_{1 \rightarrow 2}})^{s_{0 \rightarrow 3}/s_{1 \rightarrow 2}} = I_{feature}(s_0), \quad (10)$$

212 where  $I_{feature}(s_0)$  is the CRISM or OMEGA I/F value corrected for gas absorption, provided that  
 213 all assumptions inherent in the volcano-scan correction are valid.

## 214 2.3 Radiative Transfer Modeling

215 Our radiative transfer modeling utilized a publically available general purpose Fortran  
216 program for discrete-ordinate-method radiative transfer in scattering and emitting layered media,  
217 Discrete Ordinate Radiative Transfer (DISORT) [*Stamnes et al.*, 1988; *Thomas and Stamnes*,  
218 2002]. The atmosphere is treated as a plane-parallel medium in which individual layers are  
219 homogenous but interlayer properties can be varied. Attenuation and scattering of the solar  
220 beam down through the atmosphere, interaction with the surface, and attenuation and scattering  
221 up through the atmosphere are modeled. The numerical implementation is discussed in *Stamnes*  
222 *et al.*, [1999] and *Thomas and Stamnes* [2002]. Gas absorptions from CO<sub>2</sub>, CO, and H<sub>2</sub>O were  
223 defined using correlated-k distributions with parameters derived from the HITRAN database  
224 [*Rothman et al.*, 2005].

225 We utilized ‘front-end’ routines optimized for study of the Martian atmosphere,  
226 DISORT\_multi, to compute modeled CRISM and OMEGA I/F spectra [*Wolff et al.*, 2009].  
227 Atmospheric temperature profiles relevant to atmospheric conditions at the latitude, longitude,  
228 and Ls of interest were derived from spatially binned Mars Global Surveyor Thermal Emission  
229 Spectrometer (TES) observations of Mars acquired between 1998 and 2000 [*Smith*, 2004]. Dust  
230 aerosol single scattering albedos for 1.5  $\mu\text{m}$  particles and wavelength dependent phase functions  
231 utilized in our modeling were derived from analysis of CRISM hyperspectral data [*Wolff et al.*,  
232 2009]. DISORT modeled I/F spectra presented in this paper are similar to those that would be  
233 observed at the top of the Martian atmosphere by CRISM or OMEGA. Similar procedures were  
234 described by *Arvidson et al.* [2006]. Absorption, emission, and multiple scattering from  
235 atmospheric gases and aerosols were modeled.

### 236 3. Volcano-Scan Correction Simulation Results

237 To evaluate the validity of assumptions implicit in deriving empirical transmission  
238 spectra and to identify and determine causes of artifacts introduced by application of the  
239 volcano-scan correction, we simulated the volcano-scan correction using DISORT radiative  
240 transfer modeling. Comparing volcano-scan corrected spectra generated using simulated  
241 transmission spectra applied to modeled surface spectra enables identification and  
242 characterization of artifacts introduced by the volcano-scan correction without the ambiguity  
243 inherent in real data because all variables can be controlled and systematically varied. In this  
244 section, we assessed potential artifacts that could arise from variation in surface spectral features  
245 and atmospheric dust aerosols present in high and low altitude spectra used to generate empirical  
246 transmission spectra as well as from ranges of exponential scaling factors potentially used during  
247 application of the volcano-scan correction.

### 248 **3.1 Simulation of CRISM and OMEGA Empirical Transmission Spectra**

249 In order to demonstrate that simulated transmission spectra are similar to actual CRISM-  
250 and OMEGA-derived transmission spectra, our initial simulation results were aimed at  
251 approximating measured high and low altitude Olympus Mons spectra. Although we modeled  
252 empirical transmission spectra that appear similar to both CRISM and OMEGA empirical  
253 transmission spectra (Figure 3), we focus on CRISM results. The higher spectral resolution of  
254 CRISM data (Figure 1) allows for more detailed characterization of artifacts. In addition, the  
255 volcano-scan correction as applied to CRISM spectra has the added complication of a  
256 temperature dependent wavelength shift, which we explore.

257 We chose to model CRISM high and low altitude spectra of Olympus Mons from  
258 FFC000061C4. Figure 2a shows that the high and low altitude CRISM spectra do not overlap

259 and that the summit spectrum is slightly darker than the base spectrum. The dust aerosol  
260 contribution is expected to be much less at the summit than at the base of Olympus Mons  
261 because, in a uniformly mixed atmosphere, the amount of aerosol particles is proportional to the  
262 atmospheric column density, which is much less at 20 km than 0 km altitude. Given the  
263 expected small dust aerosol contribution at the summit of Olympus Mons, we attempted to  
264 reproduce the low and high altitude spectra by modeling equivalent surface spectral properties in  
265 the high and low altitude spectra, modest dust opacity for the low altitude spectrum, and zero  
266 dust opacity for the summit spectrum. The surface spectrum was modeled as a straight line with  
267 a positive slope. It was necessary to lower the surface albedo of the high altitude spectrum by  
268 5% relative to the low altitude spectrum (shown in Figure 4b) to produce modeled base and  
269 summit I/F spectra that are similar to measured base and summit I/F spectra (Figure 3). The  
270 simulated transmission spectrum has values near 1.1 on the continuum (Figure 3b, gray line)  
271 rather than expected values of 1.0, similar to the CRISM-derived transmission spectrum (Figure  
272 2b, gray). Therefore, it was multiplicatively scaled to equal unity at wavelengths lacking gas  
273 absorption (Figure 3b, black line) as was done for the actual CRISM-derived transmission  
274 spectrum (Figure 2b, black line).

275 We produced simulated transmission spectra that appear broadly similar to actual  
276 CRISM- and OMEGA-derived transmission spectra (Figure 3c, d). Volcano-scan corrections  
277 using the simulated transmission spectra shown in Figure 3 were applied to modeled low altitude  
278 Olympus Mons spectra in order to demonstrate that our simulated volcano-scan correction results  
279 are similar to CRISM and OMEGA volcano-scan corrected spectra (Figure 4). Gaussian noise  
280 with a standard deviation of 1% was added to the modeled I/F spectrum prior to application of  
281 the volcano-scan correction to make the results more realistic. The resulting simulated volcano-

282 scan corrected spectra shown in Figure 4 are similar to actual CRISM and OMEGA volcano-scan  
283 corrected spectra shown in Figure 1. The bowl-shape evident at 2000 nm (Figure 4) is similar to  
284 the bowl-shaped artifact observed in CRISM and OMEGA volcano-scan corrected spectra  
285 (Figure 1) even though the modeled input spectrum was linear (Figure 4b, c gray line). This  
286 indicates that our simulation results are sufficient to characterize artifacts introduced by the  
287 volcano-scan correction.

288

### 289 **3. 2 Impact of Aerosols and Surface Contributions in Transmission Spectra on the 2000 nm** 290 **Bowl-Shaped Artifact**

291 Two assumptions in empirically derived transmission spectra are that surface  
292 contributions to low and high altitude spectra used to create transmission spectra are equivalent  
293 and aerosol contributions to low and high altitude spectra can be ignored. If these assumptions  
294 are valid, then spectral contributions should be equivalent outside wavelengths of gas absorption  
295 in the low and high altitude spectra, and the base and summit spectra should overlap at these  
296 wavelengths, resulting in empirical transmission spectra having values of unity outside of gas  
297 absorptions. This is not the case (Figure 2a) and CRISM empirical transmission spectra must be  
298 multiplicatively scaled so that continuum values are near unity (Figure 2b). The transmission  
299 spectrum simulation results shown in Figure 4, in which the 2000 nm bowl-shaped artifact is  
300 evident, were generated to appear similar to CRISM and OMEGA data and had variable surface  
301 albedos (but no absorption feature at 2000 nm) and aerosol opacities between base and summit  
302 spectra.

303 In order to determine whether or not surface spectral features and atmospheric dust  
304 aerosols present in the high and low altitude spectra used to generate empirical transmission



305 spectra are responsible for the 2000 nm bowl-shaped artifact in the corrected spectra, we show  
306 simulation results in which these two variables are equivalent in the low and high altitude  
307 spectra. Figure 5a shows simulation results in which the base and summit spectra were identical  
308 (assumption 1 satisfied) and aerosol opacities were identical. The 2000 nm bowl-shaped artifact  
309 is evident. Figure 5b shows a similar simulation in which no aerosols were modeled (both  
310 assumption 1 and 2 satisfied). This simulation demonstrates that a 2000 nm bowl-shaped  
311 artifact occurs independently of the presence of aerosols and surface variability in the high and  
312 low altitude spectra used to generate empirical transmission spectra. Although a surface  
313 absorption feature near 2000 nm present in the base or summit spectrum could contribute to a  
314 2000 nm artifact, such a feature is not required to explain the observed 2000 nm bowl-shaped  
315 artifact in CRISM volcano-scan corrected spectra (Figure 1). However, it is important to note  
316 that variable aerosol contributions between the empirical transmission spectrum and the  
317 spectrum to be corrected causes a mismatch in shape between gas bands that results from aerosol  
318 scattering into gas lines. This mismatch in shape between gas bands in the transmission  
319 spectrum and the spectrum to be corrected causes additional artifacts near 2000 nm (section 4).

320

### 321 **3. 3 Impact of Exponential Scaling Factor on the 2000 nm Artifact**

322 The gas absorption coefficient ( $k$ ) is assumed to be constant (equation 2) in the  
323 calculation of the empirical transmission spectra. The volcano-scan correction is enabled by this  
324 assumption (equations 4-8). During the application of the volcano-scan correction, the empirical  
325 transmission spectrum is scaled exponentially by a single (wavelength independent) exponential  
326 scaling factor that is calculated so that the strength of its strong CO<sub>2</sub> absorption near 2010 nm is  
327 similar in strength to the same CO<sub>2</sub> feature in the spectrum to be corrected so that CO<sub>2</sub>

328 absorptions can be divided out (see section 2.2). Small changes to the value of the exponential  
329 scaling factor alter the expressions of the artifacts observed near 2000 nm in volcano-scan  
330 corrected spectra (Figure 6). In the absence of artifacts, too small of an exponential scaling  
331 factor would result in a residual CO<sub>2</sub> triplet near 2000 nm and too large of a scaling factor would  
332 result in an inverse triplet. Applying the scaling factor calculated using the BD1 estimate results  
333 in ‘hash’ superimposed on the bowl-shaped artifact near 2000 nm caused by over correction of  
334 some parts of the CO<sub>2</sub> triplet, even though under correction of weaker CO<sub>2</sub> bands is evident at  
335 other wavelengths (Figure 6). Applying the scaling factor calculated using the BD2 estimate  
336 results in under correction of the CO<sub>2</sub> triplet near 2000 nm that has the appearance of a deeper  
337 bowl-shape (Figure 6). This is because the BD2 estimate results in a consistently smaller  
338 calculated exponential scaling factor. The addition of noise to the simulation (Figure 6b) reduces  
339 the structured appearance of the residual gas bands but does not mask them. Similar artifacts are  
340 evident in volcano-scan corrected CRISM spectra that were corrected using variable scaling  
341 factors (Figure 6c), and there does not appear to be a single exponential scaling factor that  
342 mitigates both the ‘hash’ and bowl-shape near 2000 nm (Figures 6).

343         The variable appearance of the artifact at 2000 nm in simulated and actual volcano-scan  
344 corrected spectra caused by using different exponential scaling factors to scale the transmission  
345 spectrum prior to its division demonstrates that assumption 3 is invalid and causes a prominent  
346 artifact at 2000 nm and smaller artifacts at other wavelengths of CO<sub>2</sub> absorption. Gas bands that  
347 appear broad at CRISM and OMEGA spectral resolution contain many individual absorption  
348 lines which have variable strengths (Figure 7a). Larger absorption coefficients and/or more  
349 molecules (higher column density) in the path length result in stronger and broader lines. A  
350 detailed discussion of gas line broadening and the curve of growth in the context of radiative

351 transfer modeling can be found in *Thomas and Stamnes*, [2002]. In the weak line limit ( $\tau \ll 1$ ),  
352 or linear regime, wings of individual lines do not completely overlap and the absorptance ( $1 - T$ )  
353 is proportional to the amount of absorbing molecules. In the strong line limit ( $\tau \gg 1$ ), or  
354 saturated regime, there is a square root dependence on column density. In between these two  
355 limits, the wings of the gas lines overlap but the gas lines do not saturate, the absorption  
356 coefficient ( $k$ ) is constant with column density, and an exponential relationship between  
357 absorptance and column density is observed. This regime is described by the integrated form of  
358 the Beer-Lambert Law in which  $k$  is assumed to be constant for each wavelength (equation 2).  
359 According to equation 3,  $-\ln(T)$  should be linearly proportional to the path length,  $s$ , with the  
360 slope equal to  $k$ . A plot of  $T$  calculated for different path lengths through the atmosphere using  
361 DISORT reveals that  $T$  is not necessarily linearly proportional to  $s$  for all  $s$  for all wavelengths  
362 (Figure 7b). This result is expected because multiple regimes are experienced for the range of  
363 pressures in the Martian atmosphere and occur over different path lengths depending on the  
364 strength of  $\text{CO}_2$  absorption at a given wavelength.

365

#### 366 **4. Artifacts and Residual Atmospheric Spectral Features in CRISM Volcano-Scan** 367 **Corrected Spectra**

368 The volcano-scan correction does not specifically address potentially large spectral  
369 contributions from spatially and temporally variable dust aerosols, ice aerosols, and water vapor  
370 that are present in the Martian atmosphere. In addition, the appearance of the 2000 nm bowl-  
371 shaped artifact has variable expression depending on options selected in CAT during application  
372 of the volcano-scan correction and the temperature dependent wavelength shift of the  
373 transmission spectrum relative to the corrected spectrum. We assessed sensitivity to atmospheric

374 dust aerosols, ice aerosols, and water vapor and also present examples showing how the  
375 temperature dependent wavelength shift, band depth estimate (BD1 or BD2), and empirical  
376 artifact correction options present in CAT further impact the 2000 nm bowl-shaped artifact in  
377 CRISM spectra.

378

#### 379 **4.1 Residual Atmospheric Dust Aerosol Features**

380 Dust and ice aerosol abundances are spatially and temporally variable on Mars. Higher  
381 dust opacities are typically observed in the Martian perihelion season and there is regional  
382 variation in dust loading in the atmosphere [e.g., *Smith et al.*, 2004]. In the NIR, dust aerosols  
383 generally impart a negative slope, affect overall spectral brightness, and impact the depth and  
384 shape of the CO<sub>2</sub> triplet (Figure 8). Because multiple scattering from dust aerosols brightens  
385 dark spectra and darkens bright spectra (Figure 8), with the magnitude of the effect depending on  
386 dust opacity, the overall brightness of volcano-scan corrected spectra is not equivalent to surface  
387 albedo. This is especially evident in simulated volcano-scan corrected spectra in which the  
388 modeled surface spectrum is compared with the volcano-scan corrected spectrum (Figure 5a).  
389 The simulated volcano-scan corrected spectrum has a lower albedo and a more negative slope as  
390 a result of uncorrected dust aerosol contributions.

391 Variable aerosol contributions between the empirically-derived transmission spectrum  
392 and the spectrum to be corrected cause a mismatch in shape between gas bands, which results  
393 from aerosol scattering into gas lines. This mismatch in shape between gas bands in the  
394 transmission spectrum and the spectrum to be corrected causes additional artifacts near 2000 nm.  
395 The effect of dust aerosols on the CO<sub>2</sub> bands is most pronounced in higher opacity images  
396 because empirical transmission spectra are derived from images with low dust opacities.

397 Volcano-scan corrected high opacity spectra exhibit additional ‘hash’ near 2000 nm because of  
398 the larger mismatch in shape between gas bands in the transmission spectrum and the spectrum  
399 to be corrected. This is evident in Figure 9 in which volcano-scan corrected CRISM spectra  
400 from the same location on Mars but acquired at different times with variable atmospheric  
401 conditions are compared. For this comparison, we chose images covering the dusty plains a few  
402 km to the south of the Mars Exploration Rover Spirit landing site at Gusev crater. Surface  
403 spectra of dusty surfaces are relatively featureless in the NIR, which allows atmospheric residual  
404 features to stand out in volcano-scan corrected spectra. Multiple images were acquired of this  
405 area at different times of year that capture a variety of atmospheric dust aerosol optical depths.  
406 In addition, aerosol optical depth measurements derived from Spirit Pancam observations have  
407 been reported [Lemmon *et al.*, 2004]. The 2000 nm bowl-shaped artifact has a variable  
408 appearance in example spectra from all three images (Figure 9). Variations are evident that  
409 result from different atmospheric conditions and different volcano-scan correction options. All  
410 spectra shown in Figure 9 were corrected using transmission spectra with the closest match to the  
411 wavelength shift. Both the BD1 and BD2 estimates were used to scale the transmission spectra  
412 and the CAT empirical 2000 nm bowl-shaped artifact correction was applied (Figure 9).  
413 Volcano-scan corrected spectra from the dustiest image (FRT000553B) exhibit more ‘hash’ in  
414 the 2000 nm artifact (regardless of CAT volcano scan options) that results from changes in gas  
415 band shape caused by aerosol scattering.

416

#### 417 **4.2 Residual Atmospheric Ice Aerosol Features**

418 Water ice aerosols also effect brightness and spectral slope but are particularly  
419 problematic because they introduce absorption features at 1500, 2000, and 2400 nm (Figure 10).

420 The depth of these features depends on the ice aerosol optical depth and grain size (e. g., *Clancy*  
421 *et al.*, 2003). Water ice aerosol opacities are highly variable and these aerosols are commonly  
422 present at high latitudes during the Martian winter but occur near the equator in the aphelion  
423 season [e.g., *Clancy et al.*, 2003].

424 In order to illustrate the appearance of uncorrected water ice aerosols, we compared  
425 volcano-scan corrected spectra from two different locations within the same image.  
426 FFC0000A3F6 was acquired over a relatively featureless, dusty area of Mars. The differences  
427 between the two spectra shown in Figure 10 result from under corrected water ice aerosols.  
428 Absorption features at 1500 and 2000 nm as well as the pronounced negative slope at  
429 wavelengths  $> 2400$  nm are evident in the lower spectrum. These water ice aerosol absorptions  
430 overlap with some features in hydrated minerals, particularly hydrated sulfates [e.g., *Cloutis et*  
431 *al.*, 2006], and can interfere with mineral identifications when present.

432

### 433 **4.3 Residual Atmospheric Water Vapor Features**

434 The volcano-scan correction scales all gases (e.g., CO<sub>2</sub>, H<sub>2</sub>O and CO) present in the  
435 transmission spectrum by the exponential scaling factor calculated using the  $\sim 2100$  nm CO<sub>2</sub> band  
436 depth estimate. Water vapor concentrations in the Martian atmosphere vary by  $L_s$ , latitude, and  
437 elevation with typical values between  $\sim 5$  and 20 precipitable  $\mu\text{m}$  [e.g., *Smith et al.*, 2008].

438 Under correction of water vapor leaves atmospheric absorption features at  $\sim 1400$ , 1900, and  
439 2600 nm that can impact diagnostic spectral features exhibited by alteration phases that occur  
440 near these wavelengths. Figure 11 shows a relatively featureless dusty surface with water  
441 absorption features present. Water vapor spectral contributions to surface spectra with alteration  
442 phases are less obviously attributable to water vapor because they overlap with mineral

443 absorption features. This is well illustrated by Figure 12 which shows volcano-scan corrected  
444 CRISM spectra from the same carbonate-bearing [Ehlmann *et al.*, 2009] location on Mars but  
445 acquired at different times under variable atmospheric conditions. The 2600 nm water vapor  
446 feature overlaps with the ~2500 nm carbonate feature and contributes to mismatches between the  
447 two different spectra of the same location. In addition, this example shows that the 2000 nm  
448 bowl-shaped artifact has a variable appearance and complicates interpretation of the ~1910 nm  
449 surface hydration feature. Spectra were corrected using transmission spectra with the closest  
450 match to the wavelength shift. Both the BD1 and BD2 estimates were used to scale the  
451 transmission spectrum and the CAT empirical 2000 nm bowl-shaped artifact correction was  
452 applied (Figure 12a). A ratio spectrum is shown to highlight the fact that apparent differences  
453 between spectra taken from the two different images are related to artifacts introduced by the  
454 volcano-scan correction as well as residual atmospheric water vapor (Figure 12b). Both  
455 FRT00003FB9 and FRT0000A09C have aerosol opacities of ~0.4 calculated using methods  
456 described by Wolff *et al.* [2009].

457

## 458 **5 Summary and Implications**

459 The empirical ‘volcano-scan’ correction [Bibring *et al.*, 1989; Langevin *et al.*, 2005;  
460 McGuire *et al.*, 2009] is widely applied to CRISM and OMEGA NIR spectra between ~1000 to  
461 ~2600 nm to remove prominent atmospheric CO<sub>2</sub> absorptions with minimal computational  
462 investment. However, detailed examination of volcano-scan corrected spectra reveals a bowl-  
463 shaped artifact that overlaps with prominent CO<sub>2</sub> features near 2000 nm. The identification and  
464 characterization of both artifacts and residual atmospheric features left by the volcano-scan

465 correction is important for the proper interpretation of CRISM and OMEGA volcano-scan  
466 corrected spectra.

467         Simulation of the volcano-scan correction with radiative transfer modeling enabled  
468 assessment of assumptions underlying this empirical method of correction. We found that the  
469 most prominent artifact, a bowl-shape centered near 2000 nm, is caused by the inaccurate  
470 assumption that absorption coefficients of CO<sub>2</sub> in the Martian atmosphere are independent of  
471 column density (Figure 7). This means that transmission is not accurately derived by the  
472 division of high and low altitude Martian spectra.

473         Expression of the 2000 nm artifact varies depending on the choice of the exponential  
474 scaling factor used to scale the empirical transmission spectrum during application of the  
475 volcano-scan correction (Figure 6). In addition, differences in aerosol scattering into gas bands  
476 between the transmission spectrum and the spectrum to be corrected also causes a mismatch in  
477 shape between gas bands that results in ‘hash’ in the 2000 nm region (Figure 9). CAT software  
478 version 7.2.1 provides an option to empirically correct the bowl-shape at 2000 nm that largely  
479 removes this feature (Figures 9 and 12). However, the performance of this correction on  
480 different types of surface spectra acquired under variable atmospheric conditions has not been  
481 quantified in the literature and variations between spectra of the same surface acquired under  
482 different atmospheric conditions are evident (Figure 12).

483         Residual atmospheric contributions caused by dust aerosols, ice aerosols, and water vapor  
484 are also observed in volcano-scan corrected spectra. Because concentrations of these  
485 atmospheric species are temporally and spatially variable, features resulting from these  
486 atmospheric contributions in volcano-scan corrected spectra are also variable. Uncorrected dust  
487 aerosols modulate the spectral slope and albedo (Figure 8) causing volcano-scan corrected



488 spectra to have inaccurate low frequency shapes (Figure 5a). Uncorrected ice aerosols, when  
489 present, result in absorptions centered at 1500 and 2000 nm and a negative slope at 2400 nm  
490 (Figure 10). Under corrected water vapor in some volcano-scan corrected spectra results in  
491 absorption features centered at 1400, 1870, and 2650 nm (Figure 11). These features are  
492 particularly problematic in spectra of alteration minerals (Figure 12).

493         The presence of artifacts and residual atmospheric features left by the volcano-scan  
494 correction can impact interpretation of volcano-scan corrected CRISM and OMEGA spectra.  
495 Because spurious features introduced by the volcano-scan correction overlap with and obscure  
496 diagnostic spectral absorptions that occur between ~1900 and ~2150 nm (e.g., Figure 12),  
497 spectral ratios are commonly performed to remove these residual features (as well as calibration  
498 artifacts). Comparison of volcano-scan corrected spectra to ratioed volcano-scan corrected  
499 spectra highlights artifacts that are evident in unratioed spectra (Figure 12). Spectral ratios of  
500 volcano-scan corrected spectra are useful for confirming the presence of narrow absorption  
501 features caused by alteration phases. However, although spectral ratios largely remove the  
502 volcano-scan artifacts and residual atmospheric contributions, they impact low frequency  
503 spectral shape, i.e. continuum shape, and can produce spurious features that mimic spectral  
504 absorptions if an inappropriate denominator is utilized. Multiple scattering from atmospheric  
505 aerosols is both additive and multiplicative; therefore, aerosol spectral contributions are not  
506 completely removed by ratioing. In addition, the amplitude of ratio spectra is arbitrary and  
507 cannot be related to physically meaningful units. Quantitative spectral analyses that address  
508 band shape, band depth, and mineral abundances are strongly dependent on the quality of  
509 atmospherically corrected spectra. Because of the presence of spurious features and/or  
510 uncorrected atmospheric contributions in volcano-scan and ratio spectra, radiative transfer

511 modeling is necessary for quantitative analyses [e.g., *Arvidson et al.*, 2006; *McGuire et al.*, 2008;  
512 *Poulet et al.*, 2009a; *Poulet et al.*, 2009b; *Cull et al.*, 2010a; *Cull et al.*, 2010b; *Liu et al.*, 2012].

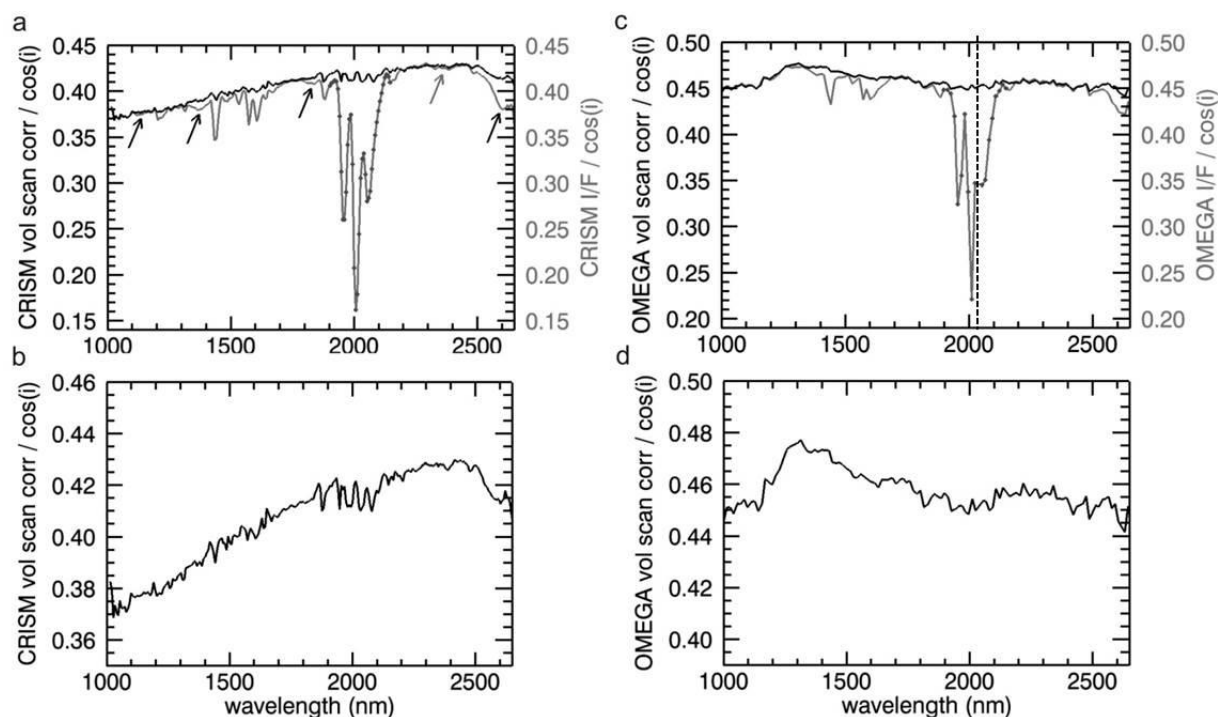
ACCEPTED MANUSCRIPT

## 513 REFERENCES

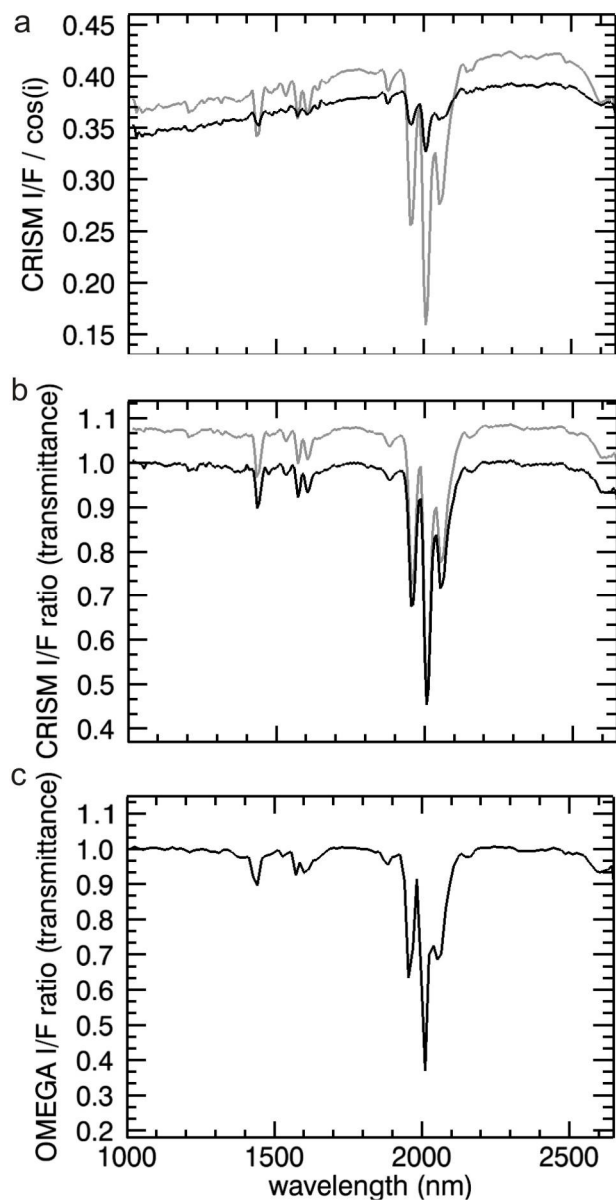
- 514
- 515 Arvidson, R. E., et al. (2006), Nature and origin of the hematite-bearing plains of Terra  
516 Meridiani based on analyses of orbital and Mars Exploration rover data sets, *J. Geophys.*  
517 *Res.*, 111, E12S08, doi:10.1029/2006JE002728.
- 518 Bibring, J.-P., et al. (1989), Results from the ISM experiment *Nature*, 341, 591-592.
- 519 Bibring, J.-P., et al. (2004), OMEGA: Observatoire pour la Minéralogie, l'Eau, les Glaces et  
520 l'Activité, in *Mars Express: The Scientific Payload*, edited by A. Wilson, Eur. Space  
521 Agency Spec. Publ., ESA SP 1240, 37-49.
- 522 Bibring, J.-P., et al. (2005), Mars surface diversity as revealed by the OMEGA/Mars Express  
523 observations, *Science*, 307, 1576-1581, doi:10.1126/science.1108806.
- 524 Clancy, R.T. et al. (2003), Mars aerosol studies with the MGS TES emission phase function  
525 observations: Optical depths, particle sizes, and ice cloud types versus latitude and solar  
526 longitude, *J. Geophys. Res.*, Research 108(E9): 5089. doi:10.1029/2003JE002058.
- 527 Cloutis, E. A., et al. (2006), Detection and discrimination of sulfate minerals using reflectance  
528 spectroscopy, *Icarus*, 184, 121-157, doi:10.1016/j.icarus.2006.04.003.
- 529 Cull, S., R. E. Arvidson, M. Mellon, S. Wiseman, R. Clark, T. Titus, R. V. Morris, and P.  
530 McGuire (2010a), Seasonal H<sub>2</sub>O and CO<sub>2</sub> ice cycles at the Mars Phoenix landing site: 1.  
531 Prelanding CRISM and HiRISE observations, *J. Geophys. Res.*, 115,  
532 E00D16, doi:10.1029/2009JE003340.
- 533 Cull, S., R. E. Arvidson, R. V. Morris, M. Wolff, M. T. Mellon, and M. T. Lemmon (2010b),  
534 Seasonal ice cycle at the Mars Phoenix landing site: 2. Postlanding CRISM and ground  
535 observations, *J. Geophys. Res.*, 115, E00E19, doi:10.1029/2009JE003410.
- 536 Ehlmann et al. (2009), Identification of hydrated silicate minerals on Mars using MRO-CRISM:  
537 Geologic context near Nili Fossae and implications for aqueous alteration, *J. Geophys.*  
538 *Res.*, 114, E00D08, doi:10.1029/2009JE003339,
- 539 Langevin, Y., F. Poulet, J.-P. Bibring, B. Gondet (2005), Sulfates in the northern polar region of  
540 Mars detected by OMEGA/Mars Express, *Science*, 307, 1584-1586.
- 541 Lemmon, M. T., et al. (2004), Atmospheric imaging results from the Mars Exploration  
542 Rovers: Spirit and opportunity, *Science*, 306, 1753-1756, doi: 10.1126/science.1104474.
- 543 Liu, Y., R. E. Arvidson, M. J. Wolff, M. T. Mellon, J. G. Catalano, A. Wang, and J. L. Bishop  
544 (2012), Lambert albedo retrieval and analyses over Aram Chaos from OMEGA  
545 hyperspectral imaging data, *J. Geophys. Res.*, 117, E00J11, doi:10.1029/2012JE004056.
- 546 McGuire, P. C. et al., (2009), An improvement to the volcano-scan algorithm for atmospheric  
547 correction of CRISM and OMEGA spectral data, *Adv. in Planet. Space Sci.*, 57,  
548 10.1016/j.pss.2009.03.007.
- 549 Murchie, S., R. E. Arvidson, P. Bendini, K. Beisser, J.-P. Bibring, J. Bishop, J. Boldt, P.  
550 Cavender, T. Choo, R. T. Clancy, E. H. Darlington, D. Des Marais, R. Espiritu, D. Fort,  
551 R. Green, E. Guinness, J. Hayes, C. Hash, K. Heffernan, J. Hemmler, G. Heyler, D.  
552 Humm, J. Hutchenson, N. Izenberg, R. Lee, J. Lees, D. Lohr, E. Malaret, T. Martin, J. A.  
553 McGovern, P. McGuire, R. V. Morris, J. F. Mustard, S. Pelkey, E. Rhodes, M. Robinson,  
554 T. Roush, E. Schafer, G. Seagrave, F. P. Seelos, IV, S. Slavney, M. Smith, W.-J. Shyong,  
555 K. Stohbehn, H. Taylor, P. Thompson, B. Tossman, M. Wirzburger, and M. Wolff

- 556 (2007), Compact Reconnaissance Imaging Spectrometer for Mars (CRISM) on Mars  
557 Reconnaissance Orbiter (MRO), *J. Geophys. Res.*, 112, E05S03,  
558 doi:10.1029/2006JE002682.
- 559 Mustard, J., et al. (2008), Hydrated silicate minerals on Mars observed by the CRISM instrument  
560 on MRO, *Nature*, 454, 305–309, doi:10.1038/nature07097.
- 561 Poulet, F., et al (2009a), Quantitative compositional analysis of martian mafic regions using the  
562 MEx/OMEGA reflectance data 1. Methodology, uncertainties and examples of  
563 application, *Icarus*, 201, 69-83, doi:10.1016/j.icarus.2008.12.025.
- 564 Poulet, F., et al (2009b), Quantitative compositional analysis of martian mafic regions using the  
565 MEx/OMEGA reflectance data 2. Petrological implications, *Icarus*, 201, 84-101,  
566 doi:10.1016/j.icarus.2008.12.042.
- 567 Rothman, L.S. et al. (2009), The HITRAN 2008 molecular spectroscopic database,  
568 *J. of Quant. Spect. Rad. Transfer*, 110, 533-572.
- 569 Smith, M.D. (2004), Interannual Variability in TES Atmospheric Observations of Mars  
570 During 1999-2003. *Icarus*, 167, 148-165.
- 571 Smith, M. D. (2008), Spacecraft Observations of the Martian Atmosphere, Annual  
572 Review of Earth and Planetary Sciences, 36, 191–219,  
573 doi:10.1146/annurev.earth.36.031207.124334.
- 574 Smith, M. D., M. J. Wolff, R. T. Clancy, and S. L. Murchie (2009), Compact Reconnaissance  
575 Imaging Spectrometer observations of water vapor and carbon monoxide, *J. Geophys.*  
576 *Res.*, 114, E00D03, doi:10.1029/2008JE003288.
- 577 Stamnes, K., S. Tsay, W. Wiscombe, and K. Jayaweera (1988), Numerically stable  
578 algorithm for discrete-ordinate-method radiative transfer in multiple scattering  
579 and emitting layered media, *Appl. Opt.*, 27, 2502-2509.
- 580 Stamnes, K., S.-C. Tsay, I. Laszlo (1999), DISORT , a general purpose Fortran program  
581 for discrete-ordinate-method radiative transfer in scattering and emitting layered  
582 media: Documentation and methodology, pp 112.
- 583 Thomas, G. E., Stamnes, K. (2002), *Radiative transfer in the atmosphere and ocean*, Cambridge  
584 University Press, New York, 546pp.
- 585 Wolff, M. J., M. D. Smith, R. T. Clancy, R. E. Arvidson, M. Kahre, F. P. Seelos  
586 IV, S. Murchie, and H. Savijarvi (2009), Wavelength dependence of dust aerosol single  
587 scattering albedo as observed by the Compact Reconnaissance Imaging Spectrometer, *J.*  
588 *Geophys. Res.*, 114, E00D04, doi:10.1029/2009JE003350.

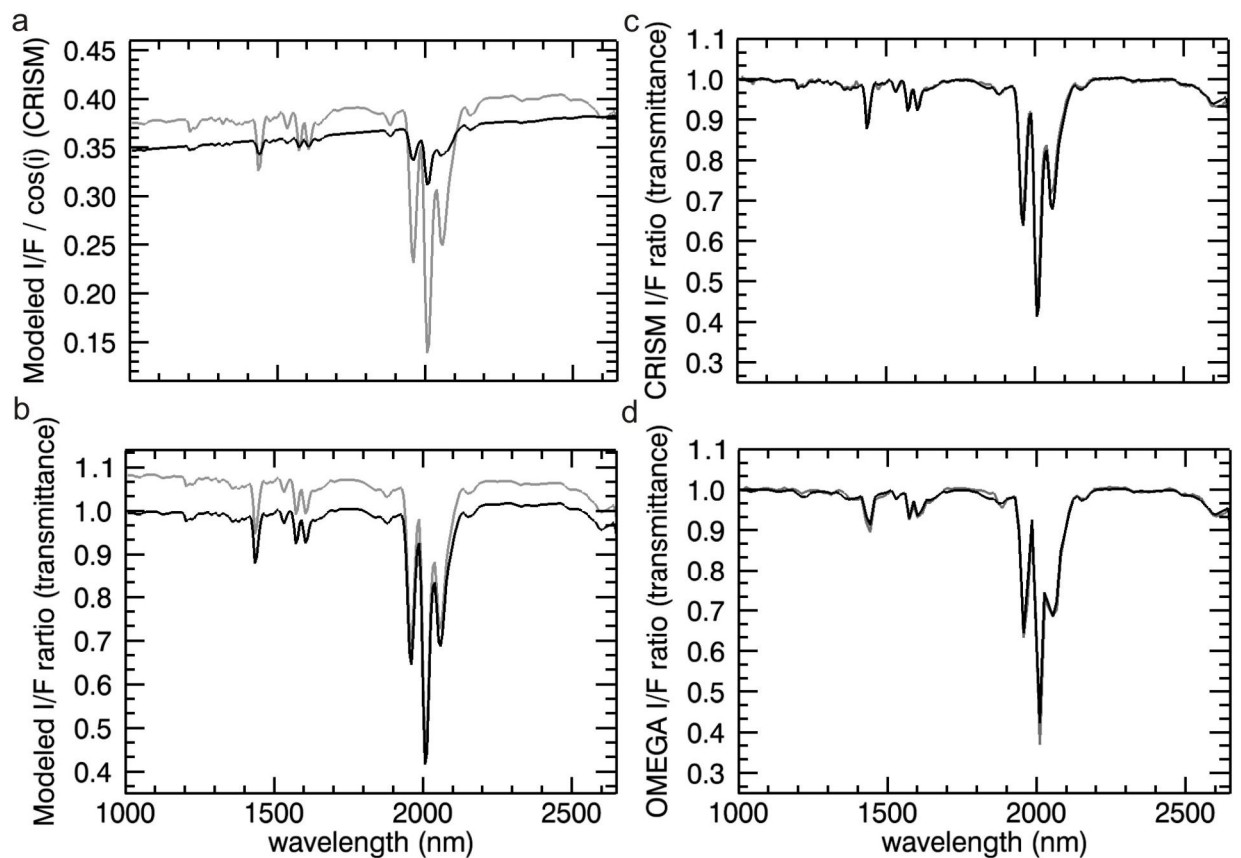
## FIGURES



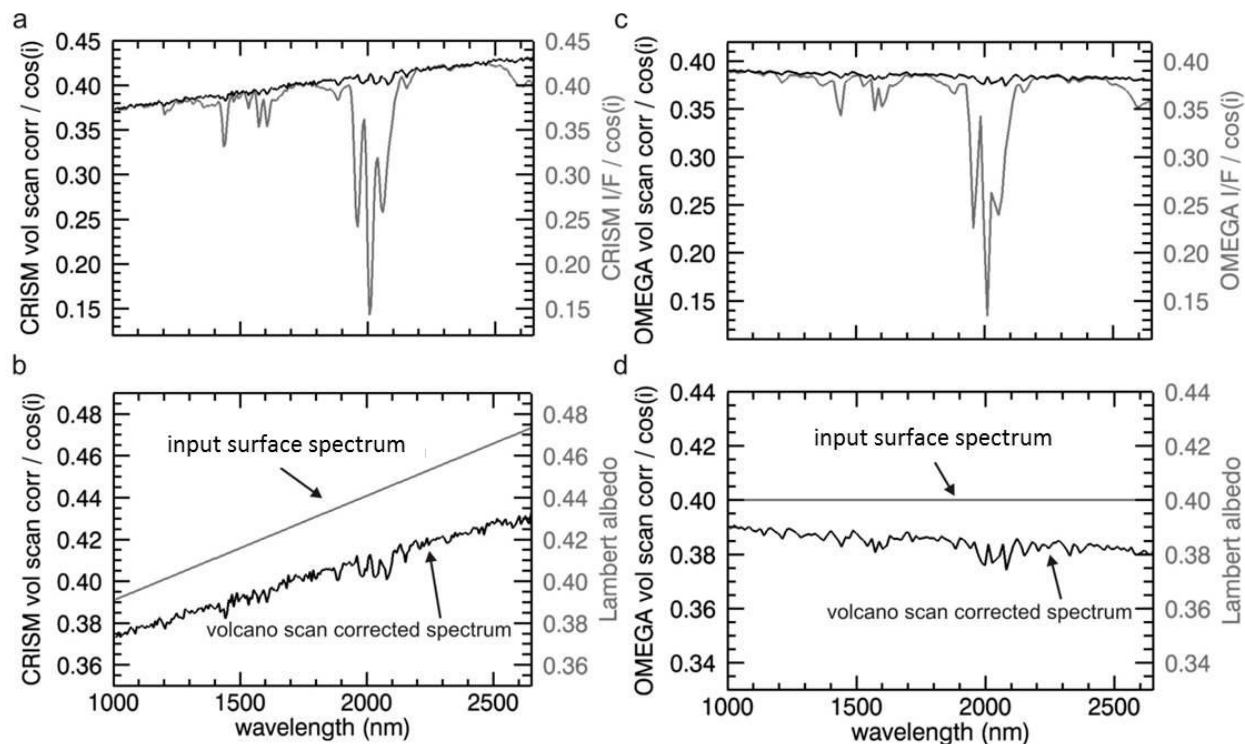
589 Figure 1. a) CRISM spectrum extracted from FFC000061C4 before (gray) and after (black)  
 590 volcano-scan correction. Because the transmission spectrum and corrected spectrum were both  
 591 derived from the same image, the temperature dependent wavelength shift is minimized. Gray  
 592 dots show CRISM channel positions located between 1900 and 2150 nm (7 nm intervals). Black  
 593 arrows indicate atmospheric H<sub>2</sub>O vapor absorptions centered near 1130, 1380, 1880, and 2590  
 594 nm. A shallow CO feature near 2350 nm is also present. Unlabeled absorptions result from  
 595 atmospheric CO<sub>2</sub>. b) Close up of the black CRISM spectrum shown in part (a). Note the bowl-  
 596 shape and ‘hash’ in the 2000 nm region. c) OMEGA spectrum extracted from ORB0037\_2  
 597 before (gray) and after (black) volcano-scan correction. Gray dots indicate OMEGA channel  
 598 positions located between 1900 and 2150 nm. OMEGA acquires data at 14 nm intervals;  
 599 however the channel at 2040 nm (dotted line) is dead. Lack of data at this wavelength causes the  
 600 longest wavelength minimum in the CO<sub>2</sub> triplet to appear less well defined in OMEGA spectra  
 601 than CRISM spectra. d) Close up of the black OMEGA spectrum shown in part (c). Both  
 602 CRISM and OMEGA spectra were extracted from dust covered surfaces located to the south of  
 603 Olympus Mons. Differences between the CRISM and OMEGA spectra shown in parts (b) and  
 604 (d) could result from calibration characteristics as well as differences in viewing geometries and  
 605 atmospheric conditions.



606  
607 Figure 2. a) CRISM high (black) and low (gray) altitude spectra acquired at the base and summit  
608 of Olympus Mons, respectively, extracted from FFC000061C4. b) CRISM scaled (black) and  
609 unscaled (gray) transmission spectra generated from low and high altitude spectra shown in part  
610 (a). c) OMEGA scaled transmission spectrum.

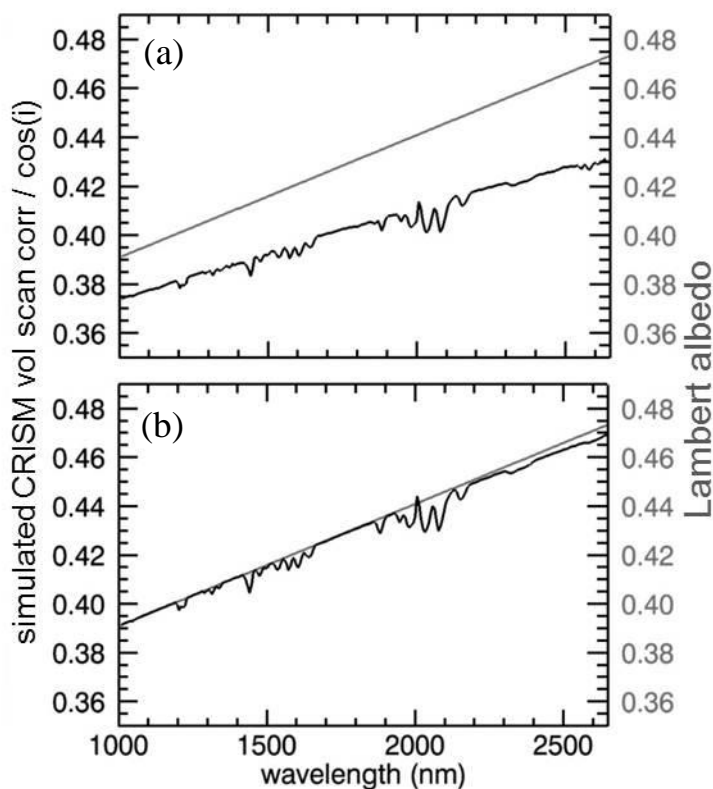


611 Figure 3. a) DISORT modeled high (black) and low (gray) altitude spectra convolved to CRISM  
 612 spectral resolution computed using pressure/temperature profiles appropriate for the base and  
 613 summit of Olympus Mons, respectively. A dust opacity of 0.3 and 5 precipitable  $\mu\text{m}$  of water  
 614 vapor were modeled for the low altitude spectrum and no dust or water vapor were modeled for  
 615 the high altitude spectrum. b) Scaled (black) and unscaled (gray) transmission spectra generated  
 616 from spectra shown in part (a). c) Modeled transmission spectrum (black) overlain on an actual  
 617 CRISM transmission spectrum (gray). d) Modeled transmission spectrum (black) overlain on an  
 618 actual OMEGA transmission spectrum (gray).

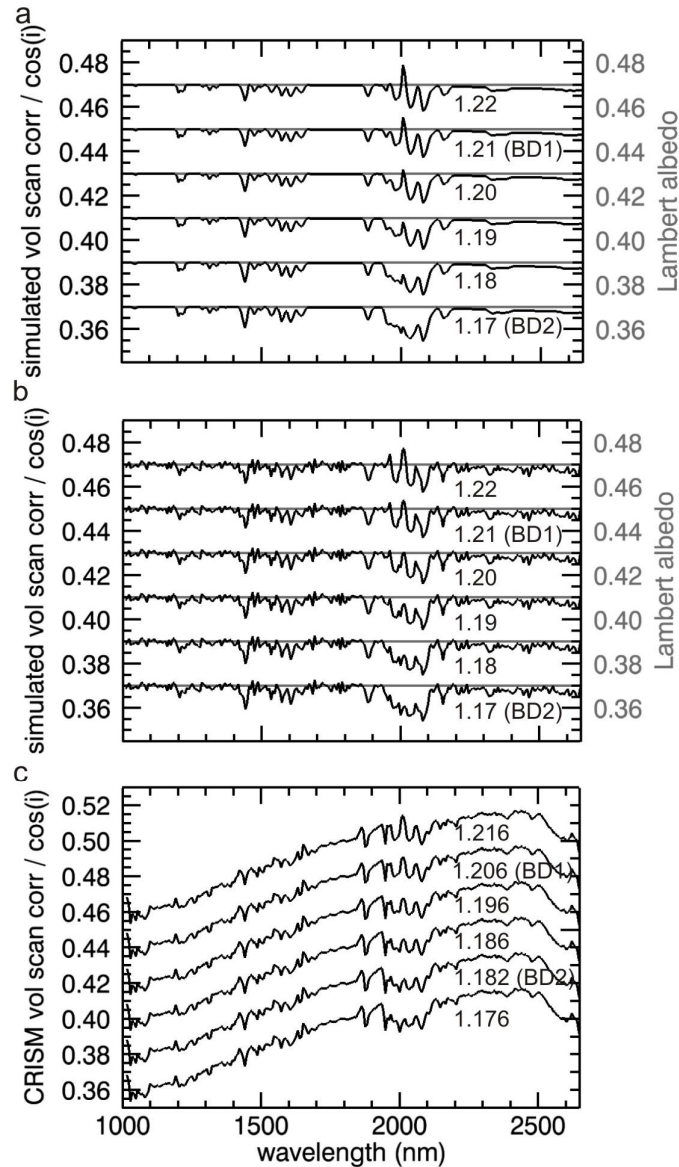


619 Figure 4. a) Modeled CRISM spectrum before (gray) and after (black) simulated volcano-scan  
 620 correction. b) Close up of the black spectrum shown in part (a) but with the input surface  
 621 spectrum over-plotted in gray. A linear function was used to model the surface spectrum to  
 622 highlight artifacts in the volcano-scan correction. Perfect atmospheric correction would result in  
 623 the black and gray spectra overlapping. c-d) Same as parts (a-b) but for OMEGA spectral  
 624 resolution. Although CRISM and OMEGA spectra shown in parts (a) and (c) were both acquired  
 625 at Olympus Mons, the CRISM spectrum has a positive slope whereas the OMEGA spectrum is  
 626 near horizontal. This mismatch in continuum shape between the two datasets, as released in the  
 627 PDS, is likely related to specifics of the instrument calibrations and is beyond the scope of this  
 628 paper to address.  
 629

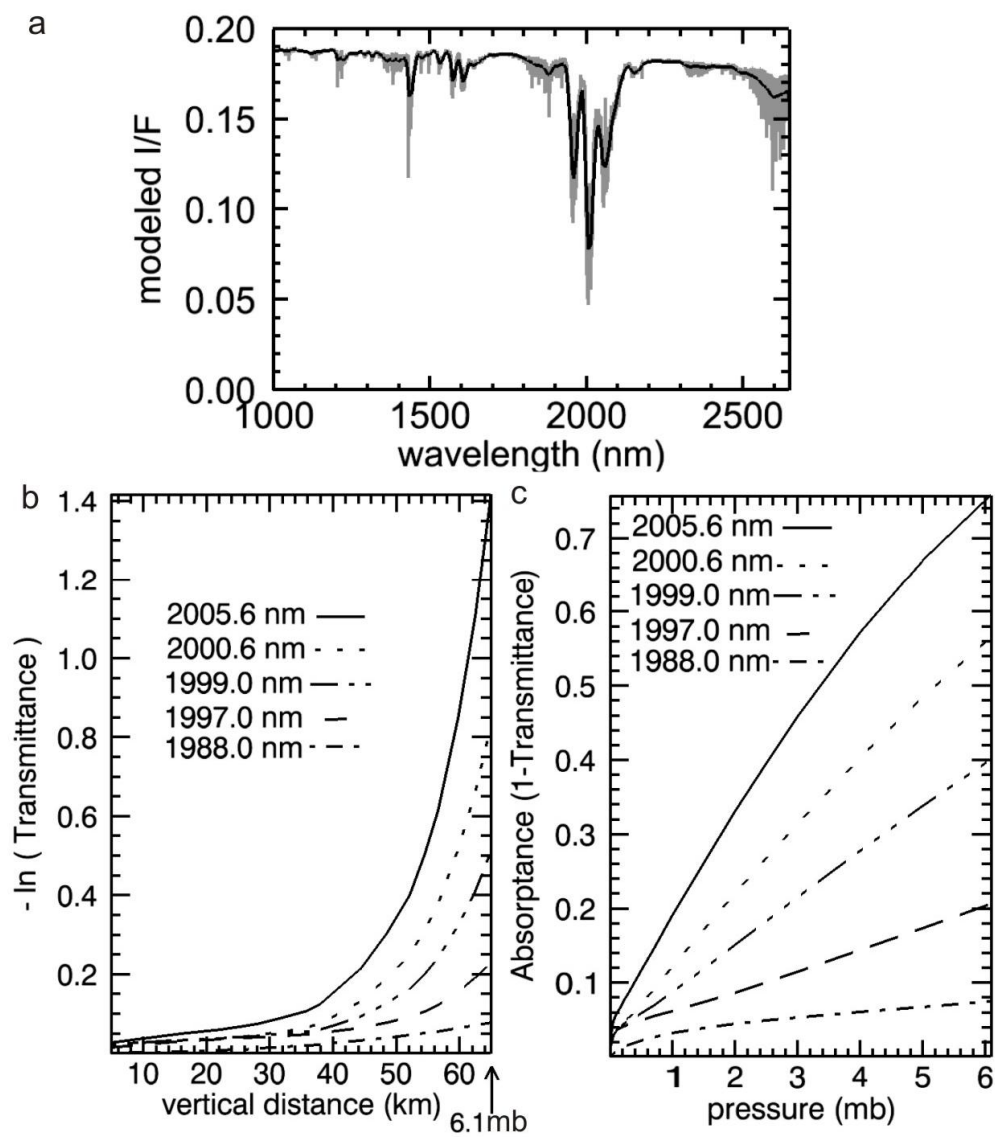




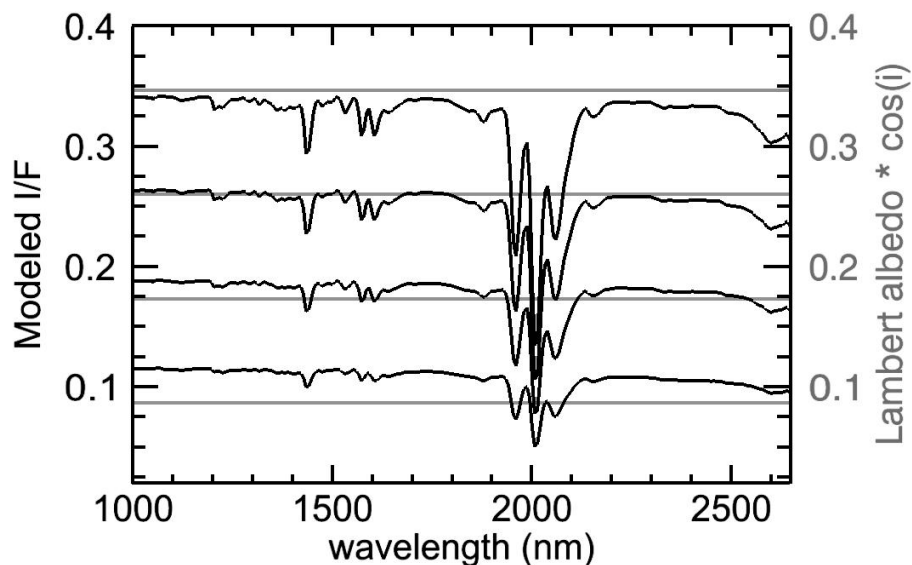
630 Figure 5. (a) Simulated CRISM volcano-scan corrected spectrum (black) and input surface  
631 Lambert albedo spectrum (gray). Aerosols were present in both the simulated transmission  
632 spectrum (Figure 3b, black) and the modeled spectrum that was corrected. Noise was not added  
633 to the simulation to highlight artifacts. Perfect atmospheric correction would result in the black  
634 spectrum overlapping with the gray spectrum. (b) Same as part (a), but with no aerosols  
635 modeled in either the simulated transmission spectrum or the corrected spectrum. Perfect  
636 atmospheric correction would result in the black spectrum overlapping with the gray spectrum.



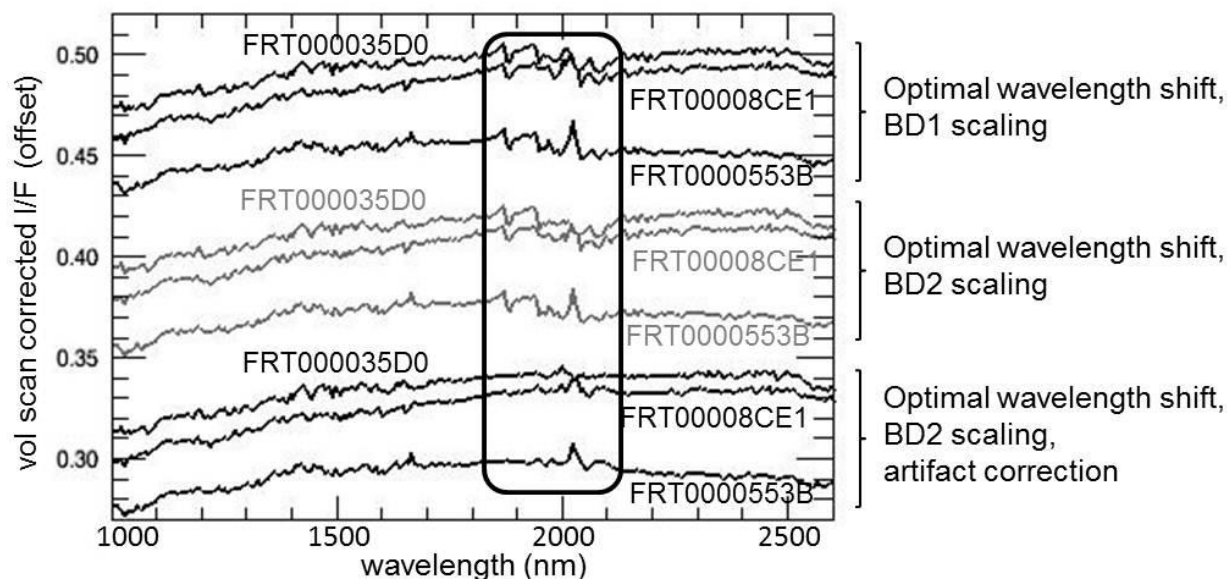
637 Figure 6. a) Black lines: Simulated volcano-scan corrected spectra using simulations with no  
 638 aerosols modeled, offset for clarity. The exponential scaling factors (see Equation 8) used to  
 639 create the simulated volcano-scan corrected spectra were systematically varied. The exponential  
 640 scaling factor used to scale the simulated transmission spectrum prior to division (labeled on  
 641 plot) was the only variable changed among the plotted spectra. Note the change in character of  
 642 the artifacts near 2000 nm as the scaling factor value is increased. The gray lines show actual  
 643 surface spectra (perfect atmospheric correction would result in the black spectra overlapping  
 644 with the gray spectra). b) Same as part (a) but with noise added. c) Actual CRISM volcano-  
 645 scan corrected spectra with systematically varied exponential scaling factors, offset for clarity.  
 646 The exponential scaling factor used to scale the transmission spectrum prior to division (labeled  
 647 on plot) was the only variable changed among the plotted spectra. Note the change in character  
 648 of the artifacts near 2000 nm as the scaling factor value is increased.



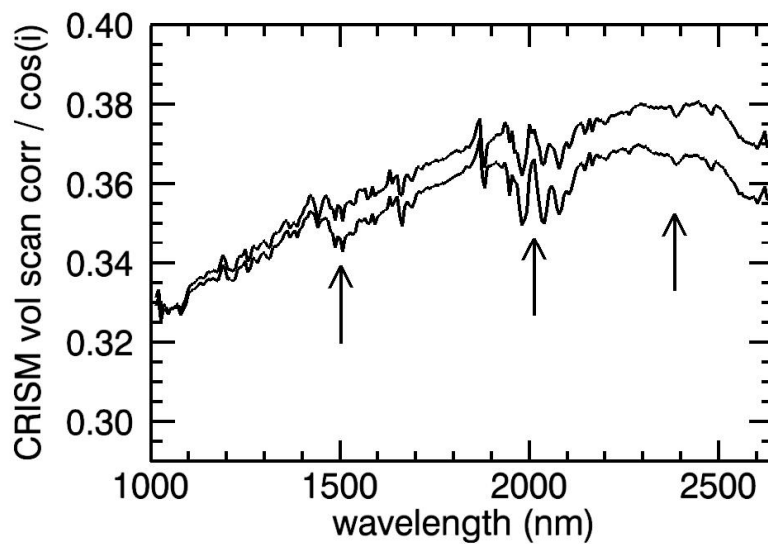
649 Figure 7. a) Shapes of gas absorption features measured by CRISM are a convolution of very  
 650 narrow gas bands and the CRISM instrument response function. Gray line: DISORT generated  
 651 I/F spectrum with I/F values calculated every 0.4 nm. Black line: High spectral resolution gray  
 652 spectrum convolved to CRISM spectral resolution. b) Plots of negative natural logarithm  
 653 transmittance calculated using DISORT versus vertical distance at several different wavelengths.  
 654 Vertical distance times 2 is equivalent to the total path length,  $s$ . According to equation 3, there  
 655 should be a linear relationship between the negative natural logarithm of transmittance and  
 656 distance,  $s$ . If this were the case, then the curves would be linear with slopes of  $k$ . For this plot,  
 657 the top of the atmosphere (vertical distance of 0) was set to 65 km above the surface, a distance  
 658 at which atmospheric pressure is negligible. At the surface (vertical distance of 65 km), the  
 659 pressure is 6.1 mb, which is Mar's average atmospheric pressure. c) Plots of absorbance versus  
 660 pressure. Pressure is exponentially proportional to vertical distance (assuming constant  
 661 temperature). Therefore, according to equation 3, these curves should also appear linear.



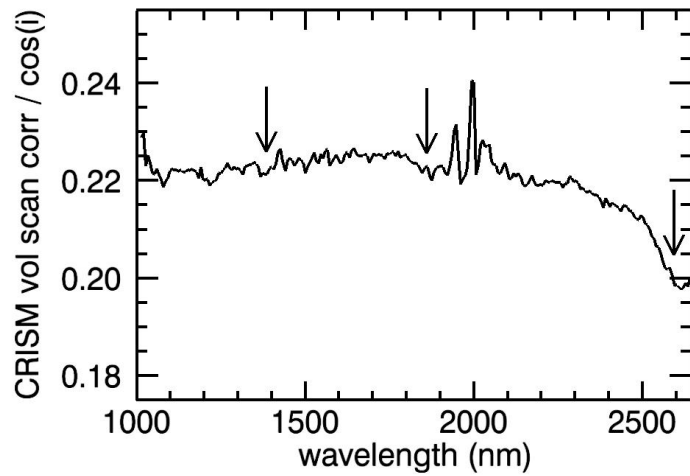
662 Figure 8. DISORT generated I/F spectra (black lines) for surface Lambert albedo spectra shown  
 663 by gray lines. Long wavelength I/F spectral shape is affected by atmospheric dust, which  
 664 imparts a negative slope. The surface Lambert albedo spectra with no atmospheric contributions  
 665 (gray lines) have slopes of 0. Multiple scattering caused by dust aerosol particles brightens I/F  
 666 spectra of dark surfaces and darkens spectra of bright surfaces. I/F spectra were modeled with  
 667 DISORT for a modest dust opacity of 0.6 at 900 nm and a viewing geometry of  $i = g = 30^\circ$ ,  $e =$   
 668  $0^\circ$  and surface Lambert albedos of 0.1, 0.2, 0.3, or 0.4 at all wavelengths.



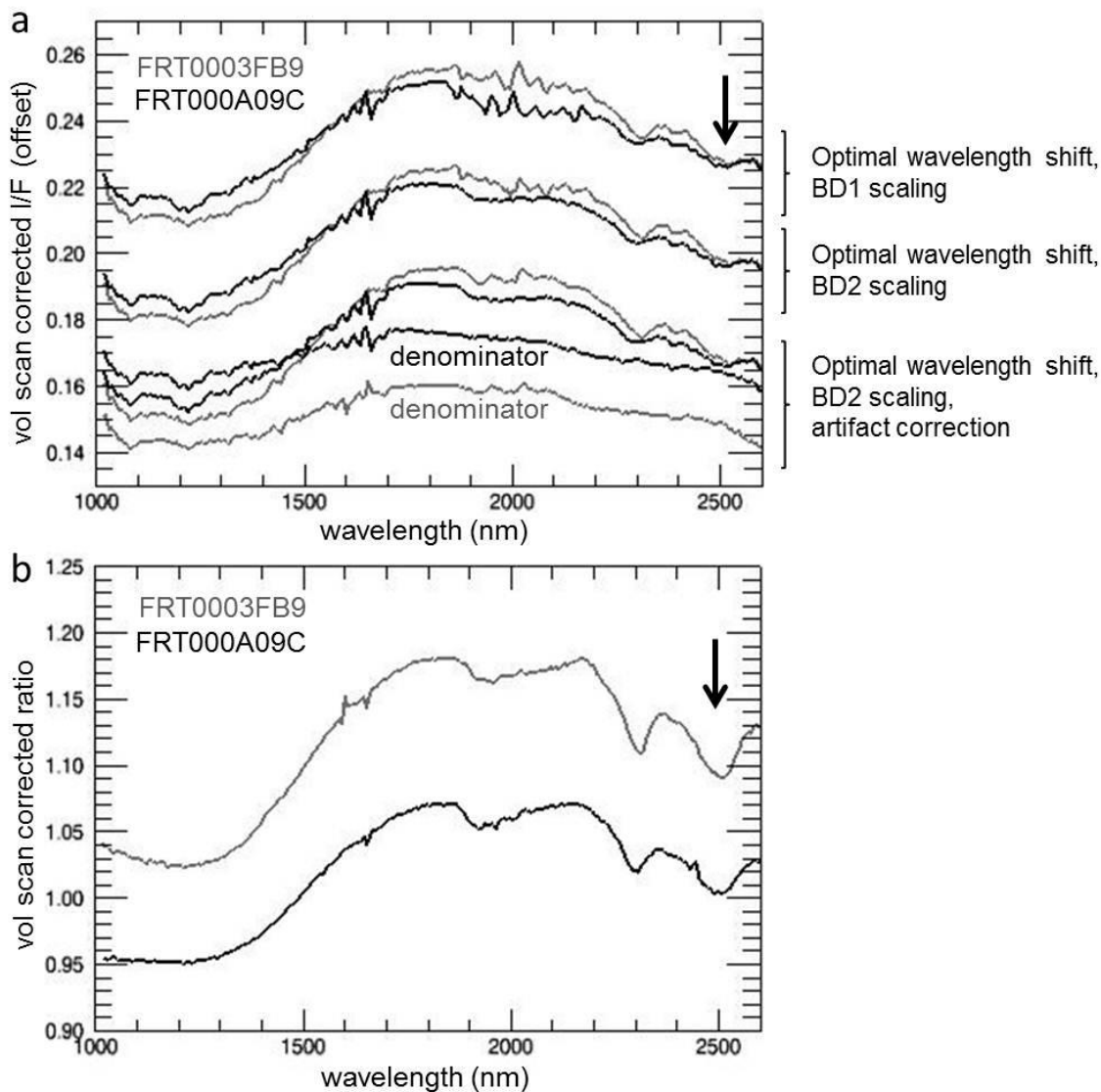
669 Figure 9. CRISM volcano-scan corrected spectra from the same location (-14.656N, 175.463E)  
 670 in Gusev crater images FRT000035D0 ( $\tau = 0.4$ ), FRT0000553B ( $\tau = 0.6$ ), and FRT00008CE1 ( $\tau$   
 671 = 0.9) (10x10 pixel average). FRT0000553B has the highest dust opacity and the most hash in  
 672 the 2000 nm bowl-shaped artifact. The 2000 nm bowl-shaped artifact has a different appearance  
 673 depending on the transmission spectrum and exponential scaling factor applied during the  
 674 volcano-scan correction.



675 Figure 10. Volcano-scan corrected CRISM I/F spectra extracted from FFC0000A3F6. The  
676 lower spectrum has distinct water ice aerosol features, which include absorptions centered at  
677 1500 and 2000 nm and a decrease in slope starting at 2300 nm. The 2000 nm ice absorption is  
678 partially obscured by artifacts induced by the volcano-scan correction.



679 Figure 11. Volcano-scan corrected CRISM I/F spectrum extracted from FRT0000CAB3 in which  
680 water vapor is under-corrected. The water vapor absorption features near 1380, 1880, and 2590  
681 nm are indicated with black arrows. Note, the CO<sub>2</sub> triplet near 2000 nm is poorly corrected as a  
682 result of high atmospheric dust opacity (> 1.0) at the time of image acquisition.



683 Figure 12. (a) CRISM volcano-scan corrected spectra from the same location (21.24N, 78.6E)  
 684 covering a carbonate- and phyllosilicate- bearing outcrop (10x10 pixel average) in Nili Fossae.  
 685 Spectra from FRT00003FB9 were extracted from column 220, line 21 and spectra from  
 686 FRT0000A09C from column 52, line 100. Although spectra were extracted from roughly the  
 687 same location, they are not expected to have identical brightnesses because of differences in  
 688 illumination resulting from different solar incidence angles and measurement emission angles.  
 689 The 2000 nm bowl-shaped artifact, which overlaps with a ~1910 nm surface hydration feature,  
 690 has a different appearance depending on the transmission spectrum and exponential scaling  
 691 factor applied during volcano-scan correction. Variable amounts of residual water vapor alter  
 692 the expression of the 2500 nm carbonate feature (black arrow). This feature looks more similar  
 693 in ratio spectra shown in part (b). (b) Spectral ratios calculated using the lower set of spectra  
 694 (optimal wavelength shift, BD2 scaling, artifact correction) shown in in part (a). Denominator  
 695 spectra used to generate these ratio spectra were extracted from the same columns as the



696 corresponding numerator spectra rather than the same surface location to minimize column  
697 dependent artifacts. Note, it was not possible to extract spectra from both the same surface  
698 location and corresponding columns as numerator spectra due to CRISM measurement geometry.  
699 Ratio spectra remove volcano-scan correction artifacts and highlight narrow absorption features.  
700 However, low frequency spectral shape is variable between numerator spectra shown in part (a)  
701 and ratioed spectra shown in part (b). In addition, the artifact correction as currently  
702 implemented in CAT v7.2.1 impacts wavelengths between ~1760 and 2240 nm and contributed  
703 to the apparent peak at ~ 2200 nm in the gray ratioed spectrum.

The empirical volcano scan correction leaves a prominent artifact near 2000nm.

Spectral albedo and slope are modified by uncorrected atmospheric aerosols.

Residual water vapor features overlap with mineral hydration features.

ACCEPTED MANUSCRIPT